Materials Research Letters

ISSN: (Print) (Online) Journal homepage: www.tandfonline.com/journals/tmrl20

Local lattice distortions and chemical short-range order in MoNbTaW

Andrea Fantin, Anna Maria Manzoni, Hauke Springer, Reza Darvishi Kamachali & Robert Maaß

To cite this article: Andrea Fantin, Anna Maria Manzoni, Hauke Springer, Reza Darvishi Kamachali & Robert Maaß (2024) Local lattice distortions and chemical short-range order in MoNbTaW, Materials Research Letters, 12:5, 346-354, DOI: 10.1080/21663831.2024.2326014

To link to this article: https://doi.org/10.1080/21663831.2024.2326014

MATER. RES. LETT.
2024, VOL. 12, NO. 5, 346–354
https://doi.org/10.1080/21663831.2024.2326014

MATERIALS RESEARCH LETTERS
Taylor & Francis
Taylor & Francis Group

ORIGINAL REPORTS

Local lattice distortions and chemical short-range order in MoNbTaW

Andrea Fantin[a,b], Anna Maria Manzoni[a], Hauke Springer[c], Reza Darvishi Kamachali[a] and Robert Maaß[a,d]

[a]Federal Institute of Materials Research and Testing (BAM), Berlin, Germany; [b]Helmholtz-Zentrum Berlin für Materialien und Energie, Berlin, Germany; [c]Max-Planck-Institut für Eisenforschung GmbH, Düsseldorf, Germany; [d]Department of Materials Science and Engineering, University of Illinois at Urbana-Champaign, Urbana, IL, USA

ABSTRACT

Extended X-ray absorption fine structure (EXAFS) conducted on an equiatomic MoNbTaW *bcc* medium-entropy alloy that was annealed at 2273 K reveals unexpectedly small 1st and 2nd shell element-specific lattice distortions. An experimental size-mismatch parameter, δ_{exp}, is determined to be ca. 50% lower than the corresponding calculated value. Around W, short-range order (SRO) preferring 4*d* elements in the 1st and 2nd shells persists. A Nb-W ordering is found, which is reminiscent of ordering emerging at lower temperatures in the B2(Mo,W;Ta,Nb)- and B32(Nb,W)-phases. With high-temperature ordering preferences in *fcc* also foreshadowing low-temperature phase, these findings suggest a general feature of high-temperature SRO.

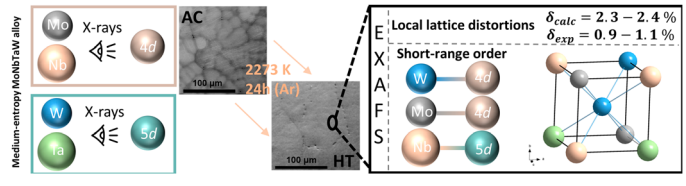

IMPACT STATEMENT

A medium-entropy MoNbTaW *bcc* alloy annealed at 2273 K shows still signs of short-range ordering which relate to its segregational behavior at lower temperatures, corroborating observations on *fcc* alloys.

ARTICLE HISTORY
Received 29 November 2023

KEYWORDS
High entropy alloys; short-range order; local lattice distortions; EXAFS; phase formation

1. Introduction

The increasing need for more specialized and better performing structural materials has driven the discovery of many remarkable alloys. The harsher the service conditions, the more specific become material demands, where for example rockets and airplane turbines belong to the most challenging environments due to extreme temperatures, corrosive gases, and mechanical forces. For example, driven by increasing energy efficiency and therefore higher engine temperatures, commercial Ni-base superalloys have undergone a tremendous many-decades-long performance development. Noticeable efforts have been made both in terms of material development and component design, the latter of which includes cooling channels or thermal barrier coatings that push application temperatures by several hundred degrees. Alongside, new base materials, including Mo-based [1,2], Nb-based [3,4], Co-based [5–8], or noble metal superalloys [9,10] have been developed. Given their limited commercial and applicational viability, the search for novel candidate alloys continues.

A promising approach has been found at the beginning of the millennium with the introduction of so-called high-entropy alloys or multi-principle element alloys [11,12], exhibiting outperforming properties beyond conventional alloy design space. One of the core effects in this novel alloy class is their configurational entropy, which allows the solid solution to be single-phase, crystallizing in simple crystal structures such as face-centered cubic (*fcc*) [11,13], body-centered cubic (*bcc*) [14,15], and to a lesser extent to hexagonal close packed (*hcp*) lattices [16].

CONTACT Andrea Fantin andrea.fantin@bam.de Federal Institute of Materials Research and Testing (BAM), Unter der Eichen 87, 12205 Berlin, Germany; Helmholtz-Zentrum Berlin für Materialien und Energie, Hahn-Meitner-Platz 1, 14019 Berlin, Germany

Supplemental data for this article can be accessed online at https://doi.org/10.1080/21663831.2024.2326014.

One of the most promising of these alloys, in terms of high-temperature properties, is the MoNbTaW alloy that was introduced by Senkov et al. in 2010 [14], and that has been studied experimentally [17–22] and with modeling [23–26] by several groups over the past decade. Investigating this alloy experimentally is a true challenge as its preparation, casting, powder metallurgical processing, as well as its homogenization, requires very high temperatures. As-cast, the alloy consistently shows segregation of the high-melting point elements W and Ta into dendritic cores, whereas the lower-melting point elements Nb and Mo segregate towards the interdendritic regions. Indeed, Senkov and co-workers [14,17] suggested these chemical fluctuations also to occur within the solid solution without having any influence on the overall lattice parameter of the alloy. Furthermore, no phase-formation was anticipated, a conclusion that to date has not been experimentally verified due to the challenges in tracking atomic-scale chemical order along very-high temperature isotherms.

However, theory and modeling have given some insights into these questions. At low temperatures ($T < 300$ K) phase separation of a B2 Mo-Ta, and a B32 Nb-W phase was predicted by theory [25,27,28], while for intermediate temperatures ($T > 350$–400 K) a B2-ordering with mixed (Mo,W) and (Nb,Ta) elements on the two sublattices [25,26,29–33] was reported. In the higher temperature regime an order–disorder transition arises [25,34], and depending on the detailed approach local order or disorder was revealed via atomistic modeling [30,31,33–36]. Considering different degrees of short- or long-range order interactions, the derived order–disorder transition temperature may vary largely (from ca. 750 K in Ref. [25] to ca. 1300 K in Refs. [25,34]), exemplifying the urgent need to validate theory and modeling with experiments.

Experimental evidence is, however, still scarce and methods to validate the theoretical findings are limited and highly specialized. One method that has proven a unique capacity in detecting local interatomic neighboring and preferences is extended X-ray absorption fine structure (EXAFS). In fact, EXAFS has recently shown that the assumed severe lattice distortion in the well-known 'Cantor' CoCrMnFeNi alloy is much less pronounced than what initially was believed [37]. Along the same line, earlier EXAFS studies on the six-component $Al_8Cr_{17}Co_{17}Cu_8Fe_{17}Ni_{33}$ (at.%) system [38,39] showed that the formation of a second Al-Cu-Ni rich $L1_2$ structured phase could be foreshadowed by the determination of preferred nearest neighbor species for Al (Al-Ni, Al-Cu) in the single-phase region. Similarly, the established preference of Cr for smaller atoms as neighbors, such as Co, Fe and Ni [39,40], was correlated with the composition of the Co-Cr-Fe rich disordered matrix forming in the two-phase region.

Here we will continue to leverage the power of EXAFS to unravel element-specific atomic ordering in the high-temperature *bcc* MoNbTaW alloy. Subjected to an unprecedented heat treatment at 2273 K for 24 h, we find that short-range order persists around W, preferring 4*d* elements in the two nearest-neighbor shells. At the same time, a Nb-W ordering is revealed that gives a strong high-temperature signature of the ordered B2 (Mo-Ta) or B32 (Nb-W) phases, otherwise associated with the medium temperature range below the order–disorder transition. This new insight suggests that high-temperature local ordering is generally indicative of lower temperature ordered phase-formation, as now established for both *fcc* and *bcc* solid solutions. Besides low temperature phase-formation predictions, modeling correctly SRO at higher temperatures may contribute in better determining its influence on dislocation behavior, as discussed for MoNbTaW [41] and similar refractory HEAs [42,43].

2. Materials and methods

The MoNbTaW was cast via arc melting and remelted four times to ensure maximum homogeneity. A heat treatment of 2273 K for 24 h in Ar was subsequently applied at the University of Bayreuth to the specimen, which was then mechanically ground and polished (200 nm sized colloidal SiO_2 suspension) for scanning-electron microscopy (SEM, Zeiss LEO 1530 with a Gemini I column), laboratory X-ray diffraction (XRD, Bruker D8 diffractometer) investigations, and synchrotron experiments. Note that the long annealing made the MoNbTaW ingot react with the ceramic support, inducing an oxygen gradient in its near-surface parts. The specimen used in the present work, approximately 1 cm^2 area × 1 mm thickness, was taken from the ingot's core. Energy dispersive X-ray spectroscopy (EDS) was performed at 5 and 20 keV, while a Cu $K\alpha_{1/2}$ radiation was employed for XRD data acquisition. The MoNbTaW sample was measured at the LISA beamline (BM08, ESRF) using a pair of Si (311) flat monochromator crystals, acquiring EXAFS spectra at Ta L_3 (9881 eV), W L_3 (10207 eV), Nb K (18986 eV), and Mo K (20000 eV) edges. Higher harmonics rejection was obtained through Si-coated (Ta, W L_3, $E_{cutoff} \approx 15$ keV) and Pt-coated (Nb, Mo K) collimating/focusing mirrors. Spectra were measured in fluorescence mode (13-channel Germanium Detector), at room temperature, employing a fixed k step of 0.05 $Å^{-1}$ up to a maximum value of about $k_{max} = 15\ Å^{-1}$, except for Ta ($k_{max} = 9.1\ Å^{-1}$) due to intrinsic range limitations because of the presence of the

Z + 1 element W (Z: atomic number) in the alloy. Data on references (Nb, Mo, W and Ta metal foils) was collected in transmission mode up to $k_{max} = 18\,Å^{-1}$.

3. Results and discussion

One of the challenges lies in the extremely high melting points of the MoNbTaW alloy (ca. 3200 K) and of all its components, above 2700 K, which implies the need for special furnaces when it comes to its homogenization. The heat treatment chosen in this study, 2273 K for 24 h, is the most extreme in terms of the combination of temperature and holding time so far for this alloy.

Figures 1(a and b) show the SEM overview images of the as-cast (AC) and the heat-treated (HT) alloy. Both states are characterized by 50–300 μm sized grains and internal segregations, with a slightly reduced segregation behavior in the HT case. 80 μm long EDS-linescans performed through one grain show relevant elemental fluctuations of Nb, Mo and W in the AC state (cf. histograms) and of W in the HT state, contrary to Ta that shows the least fluctuations and is rather uniformly distributed in the dendritic cores and in the interdendritic regions. The peak concentrations in the EDS-linescans for the AC state are especially high for Nb and W and significantly damped in the HT state. Self-diffusion and impurity diffusion data gathered from Ref. [44] allowed calculating the maximum diffusion length for all elements imposing the diffusion time (t = 24 h) as the heat-treating time (cf. Table S1, S.I.). Within 24 h and at T = 2273 K, all elements diffuse the most in Nb, between 24 (W) and 50 (Nb) µm, and the least in W, ca. 1 µm (Mo, Nb, Ta) or even less (W). These numbers are in good agreement with the experimental observation of a two-fold oscillation-period increase of the EDS line-scans between the AC and the HT state, indicating that the diffusion behavior in the MoNbTaW matrix is reasonably well extrapolated by impurity diffusion of its pure elements. Achieving a fully uniform distribution of the elements would require, however, significantly longer isotherms than pursued here,

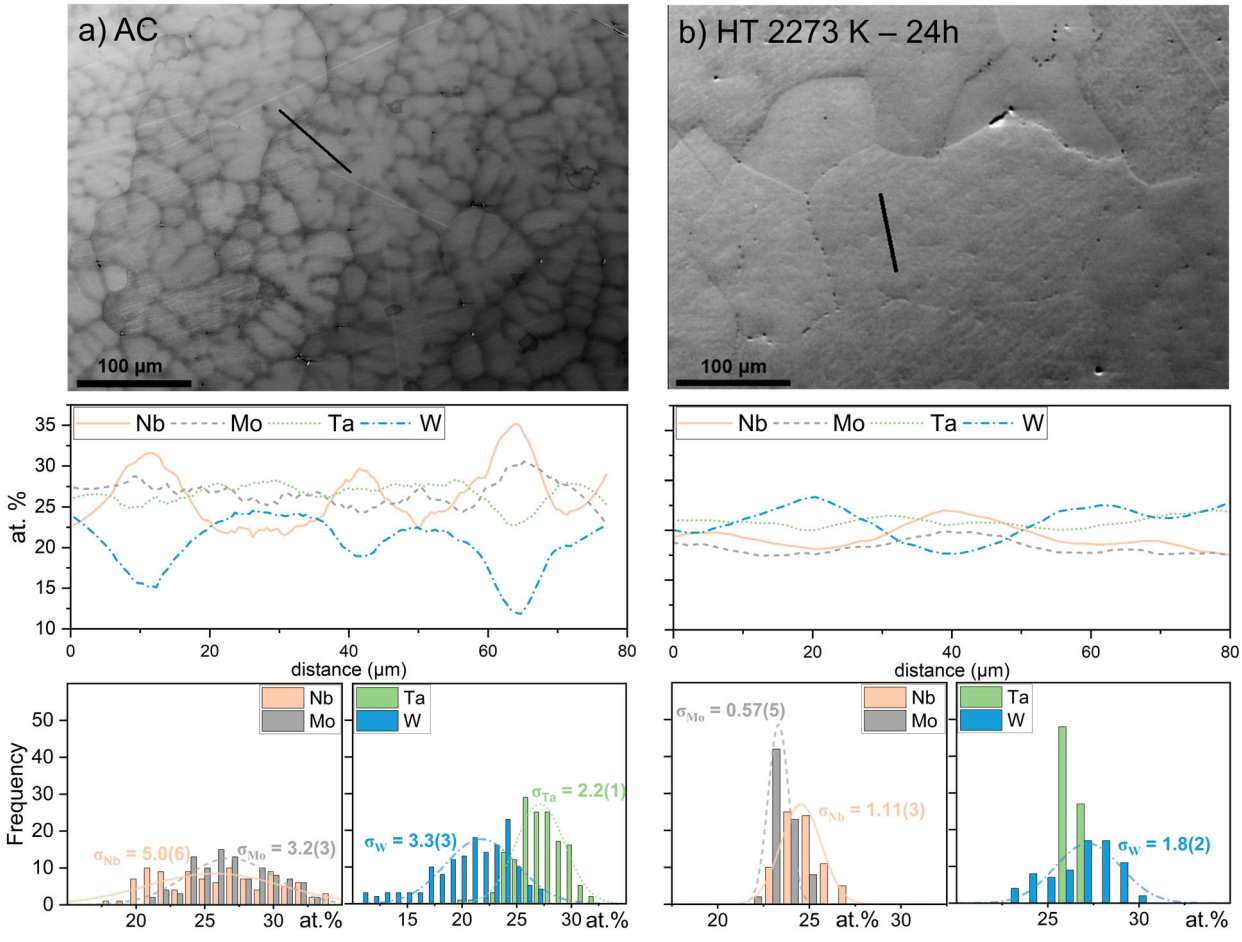

Figure 1. SEM overview and the corresponding EDS linescans with frequency histograms of (a) the as-cast MoNbTaW alloy and (b) the specimen heat treated at 2273 K, 24 h. Linescans were smoothed by Savitzky-Golay 20 p (as-cast) and 10 p (heat-treated), and frequency histograms were fitted through a normal distribution indicating the resulting standard deviation σ (in at. %), with the associated uncertainty in brackets.

which due to technical reasons was not possible. This is in line with earlier reported heat treatments, such as at 1673 K for 19 h by Senkov et al. [17] or 2073K for 7 days by Zou et al. [45], both of which were also not able to homogenize the dendritic segregation.

X-ray diffraction patterns of the AC and the HT MoNbTaW are shown in Figure 2. In Figure S1, an enlarged view of high 2θ values (HT state), together with SEM maps and optical microscopy images show the absence of secondary *bcc* phases and the remainders of a Ta-O rich segregation mainly present at the grain boundaries, undistinguishable in the XRD patterns. The refined lattice parameters using a *bcc* structure model (s.g. $Im\bar{3}m$) and the LeBail method [46] are consistent for both specimens: $a_{AC} = 3.222(1)$ Å and $a_{HT} = 3.223(1)$ Å, both of which are in good agreement with literature data on the heat-treated MoNbTaW alloy (2073 K, 7 d), $a = 3.222(1)$ Å [45]. A single *bcc* phase was indexed in Figure 2 except for a small peak at about 2θ: 72°, which is ascribed to a pure W reflection. Areas of unmolten W can be distinguished in SEM (not shown here) and are a common feature in W containing alloys. Refined lattice parameters are close to the lattice constant predicted via Vegard's law, $a_{VEG} = 3.226$ Å, and close to the 2nd shell bond distances extracted by the EXAFS analysis (reference foils' results: Table S2; MoNbTaW fits: Figure S2), presented in Table S3 together with XRD values.

In EXAFS fitting, a binary model with two gray atoms was used for modeling the spectra: one atom represents a 4*d* average, and one represents a 5*d* average, labeled 4*d* and 5*d*, respectively. According to this binary approach, 1st and 2nd shells were fitted with two paths each, defined as Abs – 4*d* and Abs – 5*d* (Abs: absorbing atom). In this way, two distances per shell are determined, the Abs – 4*d* (1st, 2nd) and Abs – 5*d* (1st, 2nd) bond lengths, depicted in Figure 3 together with the averaged 1st and 2nd shell obtained from XRD data and those obtained from the Vegard's law. The XRD 1st shell was calculated assuming that, in an undistorted *bcc* structure, the 1st shell distance is $\sqrt{3}/2a$, where a is the lattice constant. The disorder in EXAFS spectra was modeled using the Debye approximation, with only one free parameter left free, the Debye Temperature θ_D, used to compute every mean-square variation in path lengths for each path in the EXAFS fit.

By averaging the 1st shell atomic distances to nearest neighbors, a contraction of 0.8(7) % to the average 1st shell distance derived by XRD fits ($XRD_{1st} = 2.791(1)$ Å) is found. 2nd shell distances determined by EXAFS are also slightly contracted by 1(1)% compared to those determined from the XRD data. Taking a closer look, the Nb 1st shell is closest to the average structure compared to Mo, Ta and W, while Ta's 1st, 2nd and W 2nd shells are within the uncertainty of the average structure lattice value.

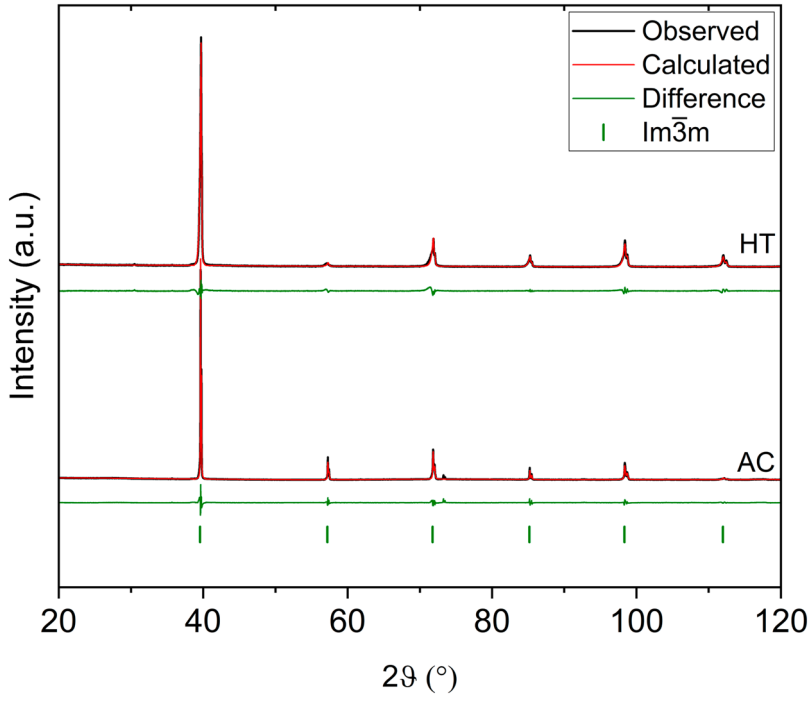

Figure 2. Observed X-ray diffraction pattern (black) of as-cast (AC) and heat-treated (2273 K–24 h, HT) together with the corresponding fit (red) and the difference of the two (green). Ticks identify the $Im\bar{3}m$ phase.

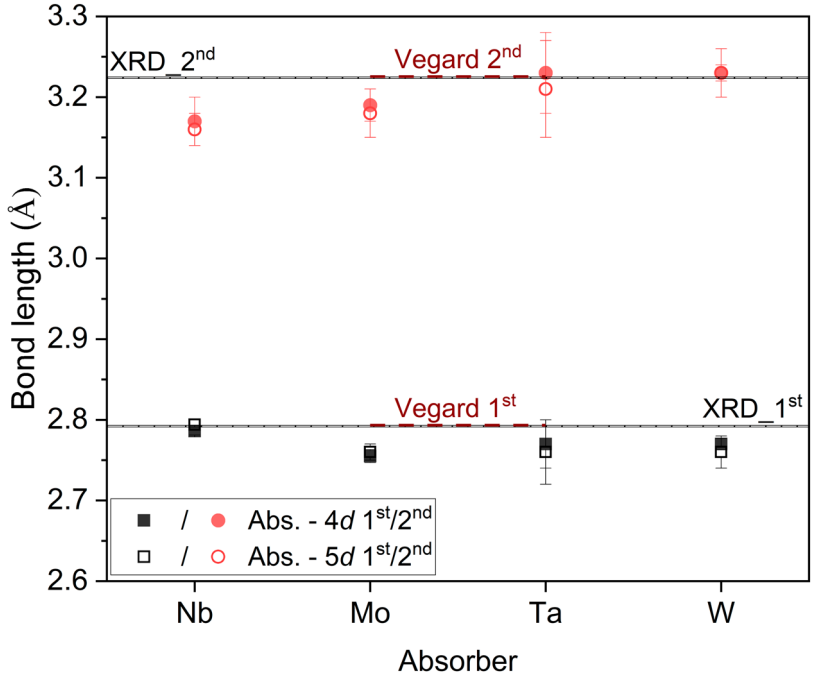

Figure 3. Comparison between XRD results (full averaged structure, lines) and EXAFS (local structure, markers), with 1st and 2nd shell distances to 4*d* (full markers) and 5*d* (empty markers), and calculations of 1st and 2nd shell distances according to Vegard's law (dashed lines).

A net distinction between local lattice distortions of *bcc* and *fcc* compounds is reported in literature [21,47,48], where it is generalized that in *bcc* the local lattice distortion distances extend up to 4 Å, compared to *fcc* systems where it remains below 3 Å. The results from Figure 4 show that the *bcc* MoNbTaW system exhibits slight distortions at least up to the 2nd shell, even though at the 1st shell level distortions are close to those found in an *fcc* alloy (0.9(2)% [39]). This hints that distortions are more related to the alloying elements' properties than to the crystal structure. MoNbTaW is reported to have a nominal low overall lattice distortion compared to several other quaternary high-entropy alloys [49,50]. A root mean square displacement (RMSD) from ideal lattice sites of ca. 0.1 Å was established by Monte Carlo/Molecular Dynamics simulations at 300 K [49], in line with the averaged value extracted from EXAFS, 0.10(1) Å. However, through EXAFS an element specific RMSD can be calculated, which spans from 0.01(3) Å (W) to 0.15(7) Å (Ta), showing that the calculated size-mismatch parameter δ_{calc} or the lattice strain index λ^*,

$$\delta_{calc} = \sqrt{\sum_{i=1}^{N} c_i \left(1 - r_i / \sum_{j=1}^{N} r_j c_j\right)^2}, \text{ and}$$

$$\lambda^* = \sqrt{\left(1 - r_i / \sum_{j=1}^{N} r_j c_j\right)^2_{max} - \left(1 - r_i / \sum_{j=1}^{N} r_j c_j\right)^2_{min}}$$

with c_i (c_j) and r_i (r_j) the relative concentration (from EDS, Table S4) and the metallic radii (from lattice parameters, Table S5) of the species $i(j)$, grasp only partially the complexity of atomic level distortions. In the interdendritic and the dendritic regions in both the homogenized and as-cast states, $\delta_{calc} = 2.3$–2.4% and $\lambda^* = 5\%$, much below the critical values of 6% and 16% [51], respectively, indicating a low elastic driving force for a phase decomposition in this alloy. The corresponding elastic energy in the homogenized state is $e = q\delta^2_{calc} = 210$ MPa [51], with $q = 2\mu\frac{(1+\nu)}{(1-\nu)} = 337$ GPa computed based on DFT calculations [52]. An experimental size-mismatch parameter δ_{exp} can also be estimated for the homogenized MoNbTaW assuming that

$$\delta_{\exp} = \sqrt{\sum_{i=1}^{N} c_{XAS}(1 - r_{EXAFS}/a_{XRD})^2}$$

with r_{EXAFS} being the observed EXAFS bond length of each absorber (cf. Table S3) and a_{XRD} is the 'average' value from XRD. c_{XAS} is the relative weight of each bond length,

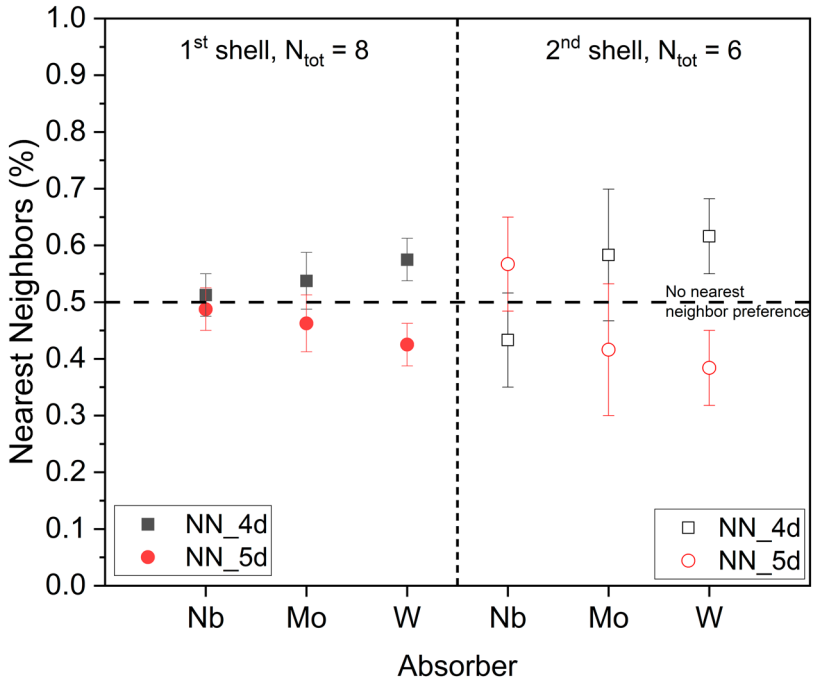

Figure 4. 1st and 2nd shells nearest neighbor (NN) preference (in %) per each absorber Nb, Mo and W, where 0.5 corresponds to a completely disordered environment.

which is assumed to be equal for every alloying element. In this way, $\delta_{exp} = 1.1\%$ (2nd shell), a ca. 50% size-mismatch decrease with respect to δ_{calc} is obtained that occurs due to the electrochemical interaction between species to stabilize the structure by reducing its distortions. EXAFS allows calculating δ_{exp} also for the 1st shell ($\delta_{exp} = 0.9\%$). Such decrease is ascribed in literature to a charge transfer [47] or electronic rearrangements including a mixture of directional bonding and metallic bonding [38–40]. Non-negligible lattice distortions in the 2nd shell also indicate the significance of ternary interactions, i.e. the additional effect of third element on pair interactions.

Simulations of MoNbTaW preferred nearest neighbors were carried out previously [30,33,35,36,41,49], indicating order at lower temperatures ($T <$ 800 K–1000 K), where intergroup near neighbor correlations remain above the inter-row correlation. These in turn remain above the self (e.g. Ta-Ta) correlations, following the proposed bond interaction strengths. For higher temperatures, the -TΔS part of the Gibbs Free Energy becomes relevant enough to substantially decrease such nearest neighbor correlations, as it can be observed for the simulations performed at 1800 K [30]. Assuming the alloy retained the structure at 2273 K before cooling, comparison with simulations should be made around this temperature, with Widom et al. [30] reporting the closest state to the present experimental conditions. Recent works [35,36] established Warren-Cowley (WC) order parameters as a function of temperature, showing that at 1773 K Ta-Mo and Nb-Mo (competition), then Ta-W and finally Nb-W pairs have negative WC parameters. Summarizing the predicted behavior of short-range order (SRO) with temperature, MoNbTaW segregates at low temperatures in B2(Mo,Ta) and B32(Nb,W) phases [25,27,28], orders into a B2(Mo,W;Ta,Nb) phase with preferred pairs above 350–400 K until an order–disorder transition occurs [25,26,29–33], above which the system slowly tends to a fully disordered solid solution. In Figure 4 is becomes evident that at 2273 K Nb has no preferences in the 1st shell and slight preferences in the 2nd shell for 5*d* metals. On the other hand, non-negligible ordering appears around Mo and W on both the 1st and 2nd shells, preferring 4*d* elements. Note that chemical fluctuations observed by SEM (μm-scale) and atomic preferences by EXAFS (Å-scale) cannot be directly related, as EXAFS resolves the SRO on much smaller length scales. As such, the effects of SEM-resolved chemical fluctuations on the SRO can essentially be neglected.

Even though EXAFS may predict only a preference to 4*d* or 5*d* elements based on the X-ray scattering contrast, theory predictions and the present experimental work may be discussed together. By combining information from the here pursued EXAFS experiments and results reported e.g. by Zhou et al. [35], He et al. [36] and/or Widom et al. [30], at the 1st shell only, the following can be deduced:

- Nb has no preference for 4*d* or 5*d* elements as its neighbors, i.e. it is surrounded by Mo and W equally.
- Mo has slight preferences for 4*d* elements over 5*d* elements, i.e. it prefers Nb over Ta, favoring Mo-Nb over the Mo-Ta pair.
- W has a clear preference for 4*d* over 5*d* elements, i.e. it prefers Nb over Ta, assumed valid for the Nb-W pair in the 2nd shell as well from both Nb and W sides.

Overall, SRO is low but non-negligible in the investigated heat-treated MoNbTaW, revealing a spatial coherence length of at least a few Å. Even though no ordered phase formation was found in this study, bonding preferences show that the modeling employed in the literature by He et al. [36] seems to predict ordering more accurately, contrarily to the smaller differences shown by Widom et al. [30]. The existence of SRO at 2273 K indicates that the mixing enthalpic energy contribution, stemming from the differences in the interatomic bond energies, is relatively strong, overcoming the entropic contribution to some extent, even at such high temperature. These results imply that an influence of the SRO on the dislocation mobility at high-temperatures might be quite different than what was reported in Yin et al. [41]. In addition, such local ordering in the alloy may act as a precursor for formation of extended ordering predicted at lower temperatures [30,33,35,36,49]. That phase formations from chemical SRO in the MoNbTaW *bcc* solid solution can be 'predicted' from a high-temperature structure, supports results obtained in previous studies on an *fcc* solid solution [39], raising the question if this is generally true. Even though this correlation is not clearly demonstrated in literature, and the present *bcc*-based with the previous *fcc*-based [39,53] studies suggest that holds true, the temperature difference in the phase diagram between measurements and lower temperature domains of second phases do play a critical role to substantiate this conclusion, and will be a matter of future investigations.

4. Conclusion

A partially homogenized, single-phase *bcc* MoNbTaW medium entropy alloy was investigated by EXAFS to determine its short-range ordering and compare it to modeling-derived phase predictions. Despite the unprecedented heat-treatment conditions used, a non-negligible amount of short-range ordering was revealed. Specifically, W shows the strongest preferential bonding behavior, i.e. it prefers 4*d* elements Nb and Mo over Ta in the 1st shell. Mo has a slight preference for Nb as its nearest neighbor while Nb is indifferent, and Ta's preferences could not be determined due to its L edges being too close to the W L edge. Despite the approximate temperature gap of 700 K between the annealing condition at T = 2273 K, and the predicted low-temperature B2(Mo,W;Ta,Nb) and B32(Nb, W) ordered phases, bonding preferences from the high 2273 K anneal (such as Nb-W) are in agreement with the expected low-temperature ordering and prove that the spatial coherence length of chemical short-range order reaches at least the 2nd shell, i.e. 3.2 Å. These results align well with earlier *fcc* high-temperature short-range ordering, suggesting that high-temperature SRO can foreshadows low-temperature ordering and phase formation.

Acknowledgements

Peter Kellner and the Chair of Ceramic Materials Engineering, University Bayreuth ceramists for the homogenizing procedure. Christiane Förster (Helmholtz-Zentrum Berlin) for help with sample preparation. A.F. gratefully acknowledges CERIC-ERIC for beamtime allocation at LISA beamline BM-08 (CRG-ESRF) and its staff (F. d'Acapito) for the continuous support. This research was carried out in part at the electron microscopy center at BAM. Romeo Saliwan Neumann and Gabriele Oder (BAM) are gratefully acknowledged.

Disclosure statement

No potential conflict of interest was reported by the author(s).

Funding

A.F. acknowledges the German Research Foundation for funding (DFG FA1817/1-2, project number: 388168974).

References

[1] Hochmuth C, Schliephake D, Völkl R, et al. Influence of zirconium content on microstructure and creep properties of Mo-9Si-8B alloys. Intermetallics. 2014 May;48:3–9. doi:10.1016/j.intermet.2013.08.017

[2] Hasemann G, Ida S, Zhu L, et al. Experimental assessment of the microstructure evolution and liquidus projection in the Mo-rich Mo-Si-B system. Mater Design. 2020 Jan;185:108233.

[3] Murakami T, Xu CN, Kitahara A, et al. Microstructure, mechanical properties and oxidation behavior of powder compacts of the Nb-Si-B system prepared by spark plasma sintering. Intermetallics. 1999 Sep;7(9):1043–1048. doi: 10.1016/S0966-9795(99)00017-5

[4] Sala K, Mitra R. Effect of Ti addition and microstructural evolution on toughening and strengthening behavior of as cast or annealed Nb-Si-Mo based hypoeutectic and hypereutectic alloys. Metall Mater Trans A. 2021 Aug;52(8):3436–3459. doi:10.1007/s11661-021-06316-3

[5] Karge L, Gilles R, Hofmann M, et al. Tac precipitation kinetics during cooling of Co-Re-based alloys. Adv Eng Mater. 2021 Nov;23(11):2100129.

[6] Rösler J, Mukherji D, Baranski T. Co-re-based alloys: a new class of high temperature materials? Adv Eng Mater. 2007 Oct;9(10):876–881. doi:10.1002/adem.200700132

[7] Pollock TM, Dibbern J, Tsunekane M, et al. New Co-based gamma-gamma high-temperature alloys. Jom-Us. 2010 Jan;62(1):58–63. doi:10.1007/s11837-010-0013-y
[8] Cao BX, Zhao YL, Yang T, et al. L1(2)-strengthened Co-rich alloys for high-temperature structural applications: A critical review. Adv Eng Mater. 2021 Oct;23(10):2100453.
[9] Sha JB, Yamabe-Mitarai Y. Saturated solid-solution hardening behavior of Ir-Hf-Nb refractory superalloys for ultra-high temperature applications. Scripta Mater. 2006 Jan;54(1):115–119. doi:10.1016/j.scriptamat.2005.08.038
[10] Wenderoth M, Vorberg S, Fischer B, et al. Isothermal oxidation behavior of a precipitation-hardened Pt-base alloy with additions of Al, Cr and Ni. Int J Mater Res. 2007 Jun;98(6):463–467. doi:10.3139/146.101498
[11] Cantor B, Chang ITH, Knight P, et al. Microstructural development in equiatomic multicomponent alloys. Mater Sci Eng A. 2004 Jul;375:213–218. doi:10.1016/j.msea.2003.10.257
[12] Yeh JW. Nano-structured high-entropy alloys. Knowledge Bridge. 2003;40:1–2.
[13] Freudenberger J, Rafaja D, Geissler D, et al. Face centred cubic multi-component equiatomic solid solutions in the Au-Cu-Ni-Pd-Pt system. Metals (Basel). 2017 Apr;7(4):135.
[14] Senkov ON, Wilks GB, Miracle DB, et al. Refractory high-entropy alloys. Intermetallics. 2010 Sep;18(9):1758–1765. doi:10.1016/j.intermet.2010.05.014
[15] Senkov ON, Scott JM, Senkova SV, et al. Microstructure and room temperature properties of a high-entropy TaNbHfZrTi alloy [Article]. J Alloy Compd. 2011 May;509(20):6043–6048. doi:10.1016/j.jallcom.2011.02.171
[16] Feuerbacher M, Heidelmann M, Thomas C. Hexagonal high-entropy alloys [Article]. Mater Res Lett. 2015;3(1):1–6. doi:10.1080/21663831.2014.951493
[17] Senkov ON, Wilks GB, Scott JM, et al. Mechanical properties of Nb25Mo25Ta25W25 and V20Nb20Mo20Ta20W 20 refractory high entropy alloys. Intermetallics. 2011 May 01;19(5):698–706. doi:10.1016/j.intermet.2011.01.004
[18] Han JS, Su B, Lu JJ, et al. Preparation of MoNbTaW refractory high entropy alloy powders by pressureless spark plasma sintering: crystal structure and phase evolution. Intermetallics. 2020 Aug;123:106832.
[19] Dobbelstein H, Thiele M, Gurevich EL, et al. Direct metal deposition of refractory high entropy alloy MoNbTaW. Phys Procedia. 2016;83:624–633. doi:10.1016/j.phpro.2016.08.065
[20] Quammen RN, Rottmann PF. Investigation of low temperature oxidation behavior of MoNbTaW thin films. J Alloy Compd. 2022 Apr 15;900:163373.
[21] Tong YG, Qi PB, Liang XB, et al. Different-Shaped ultrafine MoNbTaW HEA powders prepared via mechanical alloying. Materials (Basel). 2018 Jul;11(7):1250.
[22] Moorehead M, Bertsch K, Niezgoda M, et al. High-throughput synthesis of Mo-Nb-Ta-W high-entropy alloys via additive manufacturing. Mater Design. 2020/02/01/;187:108358. doi:10.1016/j.matdes.2019.108358
[23] Maresca F, Curtin WA. Theory of screw dislocation strengthening in random BCC alloys from dilute to "High-Entropy" alloys. Acta Mater. 2020 Jan 1;182:144–162. doi:10.1016/j.actamat.2019.10.007
[24] Maresca F, Curtin WA. Mechanistic origin of high strength in refractory BCC high entropy alloys up to 1900K. Acta Mater. 2020 Jan 1;182:235–249. doi:10.1016/j.actamat.2019.10.015
[25] Körmann F, Ruban AV, Sluiter MHF. Long-ranged interactions in bcc NbMoTaW high-entropy alloys. Mater Res Lett. 2017/01/02;5(1):35–40. doi:10.1080/21663831.2016.1198837
[26] Körmann F, Sluiter MHF. Interplay between lattice distortions, vibrations and phase stability in NbMoTaW high entropy alloys. Entropy-Switz. 2016;18(8):403. doi:10.3390/e18080403
[27] Kim AD, Widom M. Interaction models and configurational entropies of binary MoTa and the MoNbTaW high entropy alloy. Phys Rev Mater. 2023 Jun 6;7(6):063803.
[28] Blum V, Zunger A. Prediction of ordered structures in the bcc binary systems of Mo, Nb, Ta, and W from first-principles search of approximately 3,000,000 possible configurations. Phys Rev B. 2005 Jul;72(2):020104(R). doi:10.1103/PhysRevB.72.020104.
[29] Huhn WP, Widom M. Prediction of A2 to B2 phase transition in the high-entropy alloy Mo-Nb-Ta-W. Jom-Us. 2013 Dec 01;65(12):1772–1779. doi:10.1007/s11837-013-0772-3
[30] Widom M, Huhn WP, Maiti S, et al. Hybrid monte carlo/molecular dynamics simulation of a refractory metal high entropy alloy. Metall Mater Trans A. 2014 Jan 01;45(1):196–200. doi:10.1007/s11661-013-2000-8
[31] Kostiuchenko T, Körmann F, Neugebauer J, et al. Impact of lattice relaxations on phase transitions in a high-entropy alloy studied by machine-learning potentials. Npj Comput Mater. 2019 May 01;5(1):55. doi:10.1038/s41524-019-0195-y
[32] del Grosso MF, Bozzolo G, Mosca HO. Determination of the transition to the high entropy regime for alloys of refractory elements. J Alloy Compd. 2012 Sep 05;534:25–31. doi:10.1016/j.jallcom.2012.04.053
[33] del Grosso MF, Bozzolo G, Mosca HO. Modeling of high entropy alloys of refractory elements. Phys B. 2012 Aug 15;407(16):3285–3287. doi:10.1016/j.physb.2011.12.088
[34] Huhn WP. Thermodynamics from first principles: prediction of phase diagrams and materials properties using density functional theory. Carnegie Mellon University; 2018.
[35] Zhou X, He S, Marian J. Vacancy energetics and diffusivities in the equiatomic multielement Nb-Mo-Ta-W alloy. Materials (Basel). 2022;15(15):5468. doi:10.3390/ma15155468
[36] He QF, Tang PH, Chen HA, et al. Understanding chemical short-range ordering/demixing coupled with lattice distortion in solid solution high entropy alloys. Acta Mater. 2021 Sep1;216:117140. doi:10.1016/j.actamat.2021.117140
[37] Oh HS, Ma D, Leyson GP, et al. Lattice distortions in the FeCoNiCrMn high entropy alloy studied by theory and experiment. Entropy-Switz. 2016;18(9):321. doi:10.3390/e18090321
[38] Fantin A, Cakir CT, Kasatikov S, et al. Effects of heat treatment on microstructure, hardness and local structure in a compositionally complex alloy. Mater Chem Phys. 2022 Jan 15;276:125432. doi:10.1016/j.matchemphys.2021.125432

[39] Fantin A, Lepore GO, Manzoni AM, et al. Short-range chemical order and local lattice distortion in a compositionally complex alloy. Acta Mater. 2020 Jul 1;193:329–337. doi:10.1016/j.actamat.2020.04.034
[40] Kasatikov S, Fantin A, Manzoni AM, et al. Chemical interaction and electronic structure in a compositionally complex alloy: a case study by means of X-ray absorption and X-ray photoelectron spectroscopy. J Alloy Compd. 2021 Mar 15;857:157597. doi:10.1016/j.jallcom.2020.157597
[41] Yin S, Zuo YX, Abu-Odeh A, et al. Atomistic simulations of dislocation mobility in refractory high-entropy alloys and the effect of chemical short-range order. Nat Commun. 2021 Aug 11;12(1):4873.
[42] Chen S, Aitken ZH, Pattamatta S, et al. Crack tip dislocation activity in refractory high-entropy alloys. Int J Mech Sci. 2024 Jan 15;262:108753. doi:10.1016/j.ijmecsci.2023.108753
[43] Chen S, Aitken ZH, Pattamatta S, et al. Short-range ordering alters the dislocation nucleation and propagation in refractory high-entropy alloys. Mater Today. 2023 May;65:14–25. doi:10.1016/j.mattod.2023.03.009
[44] Neumann G, Tuijn C. Self-diffusion and impurity diffusion in pure metals. Amsterdam: Elsevier; 2008. (Pergamon Materials Series)
[45] Zou Y, Maiti S, Steurer W, et al. Size-dependent plasticity in an Nb25Mo25Ta25W25 refractory high-entropy alloy. Acta Mater. 2014 Feb 15;65:85–97. doi:10.1016/j.actamat.2013.11.049
[46] Le Bail A. Whole powder pattern decomposition methods and applications: a retrospection. Powder Diffr. 2005;20(4):316–326. doi:10.1154/1.2135315
[47] Meng F, Zhang W, Zhou Z, et al. Charge transfer effect on local lattice distortion in a HfNbTiZr high entropy alloy. Scr Mater. 2021 Oct 1;203:114104. doi:10.1016/j.scriptamat.2021.114104
[48] Tong Y, Zhao S, Bei H, et al. Anomalous local distortion in BCC refractory high-entropy alloys. arXiv preprint arXiv:190209279. 2019.
[49] Feng R, Liaw PK, Gao MC, et al. First-principles prediction of high-entropy-alloy stability. Npj Comput Mater. 2017 Nov 21;3(1):50. doi:10.1038/s41524-017-0049-4
[50] Romero RA, Xu S, Jian W-R, et al. Atomistic simulations of the local slip resistances in four refractory multi-principal element alloys. Int J Plast. 2022 Feb 1;149:103157. doi:10.1016/j.ijplas.2021.103157
[51] Kamachali RD, Wang L. Elastic energy of multi-component solid solutions and strain origins of phase stability in high-entropy alloys. Scripta Mater. 2022 Jan 1;206:114226.
[52] Li XG, Chen C, Zheng H, et al. Complex strengthening mechanisms in the NbMoTaW multi-principal element alloy. Npj Comput Mater. 2020 Jun 2;6(1):70.
[53] Fantin A, Lepore GO, Widom M, et al. How atomic bonding plays the hardness behavior in the Al–Co–Cr–Cu–Fe–Ni high entropy family. Small Science. 2024;4(2):2300225.